Influence of oxygen ingress on microstructure and phase formation during two-step oxidation surface hardening of TiZrNbHfTa high entropy alloy
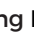
View Online   Export Citation   CrossMark

Daniel Dickes,[1] (iD) Yujun Zhao,[2] (iD) Felix Baier,[3] Beyza Öztürk,[4] (iD) Rainer Völkl,[1] Tong Li,[2] (iD) Mathias C. Galetz,[4] (iD) and Uwe Glatzel[1,a] (iD)

AFFILIATIONS

[1]Metals and Alloys, University of Bayreuth, Prof.-Rüdiger-Bormann-Straße 1, 95447 Bayreuth, Germany
[2]Institute for Materials, Ruhr University Bochum, Universitätsstraße 150, 44801 Bochum, Germany
[3]Experimental Physics XI, University of Bayreuth, Universitätsstraße 30, 95447 Bayreuth, Germany
[4]Materials and Corrosion, DECHEMA-Forschungsinstitut, Theodor-Heuss-Allee 25, 60486 Frankfurt am Main, Germany

Note: This paper is part of the APL Special Collection on Era of Entropy: Synthesis, Structure, Properties, and Applications of High Entropy Materials.
[a]Author to whom correspondence should be addressed: uwe.glatzel@uni-bayreuth.de

ABSTRACT

Aiming for an increased surface hardness and a better wear resistance of TiZrNbHfTa, we investigate a two-step process combining oxidation of rolled, ultrafine-grained, single-phase bcc TiZrNbHfTa in air at 550 °C with a vacuum heat treatment process at 1200 °C, including subsequent quenching. The first process step is associated with the formation of a surface oxide layer, a phase decomposition of the bulk, and oxygen ingress into the bulk, leading to an oxygen-enriched subsurface region containing internal oxides. The second process step is capable of restoring the single-phase nature of the bulk TiZrNbHfTa. At the same time, the presence of a compact surface oxide layer of 1–2 μm and an oxygen-enriched subsurface region underneath is preserved. The oxygen present in the subsurface region stabilizes a two-phase regime consisting of a Hf- and Zr-rich hcp phase and an Nb- and Ta-rich bcc phase, with the oxygen being interstitially dissolved predominantly in the hcp phase.

The equimolar refractory high entropy alloy TiZrNbHfTa, first presented by Senkov et al.,[1] is exceptional because it is single-phase base-centered cubic (bcc) at room temperature,[1,2] upon quenching from temperatures above 1020 °C, and still exhibits ductile behavior.[3,4] Many other favorable material properties, such as a high compressive yield strength[5,6] or a good fatigue behavior,[7] are attributed to TiZrNbHfTa. Owing to its low Young's modulus of 93.3 GPa,[4] TiZrNbHfTa is also discussed as an implant material,[8] including applications such as artificial joints. For artificial joints, high wear resistance is of utmost importance to avoid revision surgeries due to the occurrence of wear debris, which can cause inflamations.[9] To address this issue, oxidation has been studied as one method to generate a hard, adherent surface oxide layer on a TiZrNbHfTa substrate.[10]

Yet, coarse-grained TiZrNbHfTa with a grain size of approximately 50 μm or more is prone to oxide layer spallation, leading to severely degraded surfaces during high-temperature oxidation.[8,10–12] This phenomenon is also encountered in other refractory high entropy alloys.[13]

In contrast, single-step oxidation of ultrafine-grained TiZrNbHfTa in air at 550–650 °C for up to 24 h leads to the formation of a hard, adherent surface oxide layer on top of an oxygen-enriched region containing internal oxides.[10] Figure 1(a) schematically represents the temperature profile of such a single-step oxidation process. As the phase diagram in Fig. 1(b) shows and other works[14–16] confirm, the initial single-phase bcc state, herein called bcc1, is not stable in the temperature range of 550–650 °C. Instead, a phase decomposition into a Nb- and Ta-rich bcc2 and a Hf- and Zr-rich hexagonal-close packed
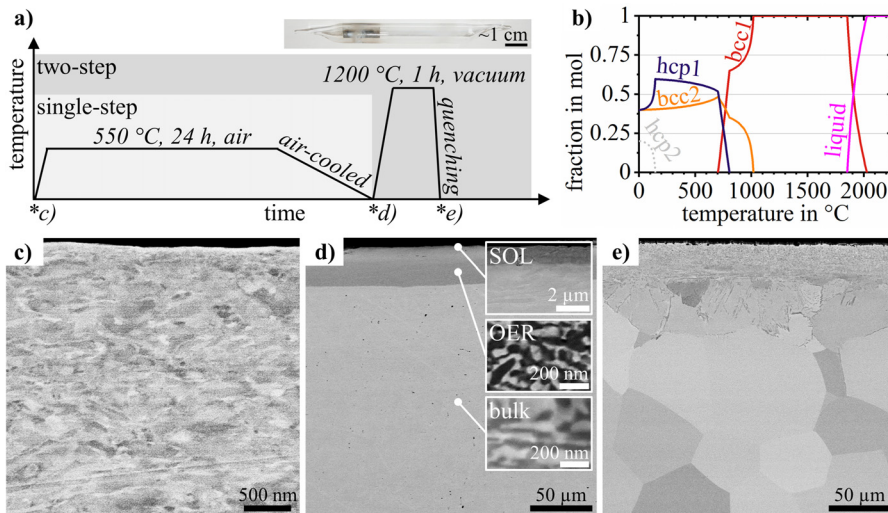
FIG. 1. (a) Schematic representation of the single-step and the two-step process with an image of the deployed quartz glass tubes and (b) TiZrNbHfTa phase diagram. (c)–(e) Backscattered SEM images revealing the microstructure of the initial state and after the single- and two-step oxidation process, as indicated in (a).

(hcp) hcp1 phase occurs.[10] Figure 1(c) shows the initial microstructure of ultrafine-grained TiZrNbHfTa cold-rolled sheet material provided by E. P. George, Oak Ridge National Laboratories. The details on the manufacturing process can be retrieved from Gadelmeier et al.[17] As visible in Fig. 1(d), single-step oxidation not only leads to the formation of a surface oxide layer (SOL) on top of an oxygen-enriched subsurface region (OER) with internal oxides but also affects the bulk material due to the phase decomposition, as discussed in our previous work.[10] Such a phase decomposition and the associated microstructure change can completely alter mechanical properties such as the hardness, strength, or ductility of the bulk material.[14,18] This is an unintended side effect when deploying single-step oxidation as a method of surface hardening. At this point, the question arises if an additional heat treatment process step can restore the initial bcc1 single-phase character of the bulk material and how it would affect the presence of the surface oxide layer and the oxygen-enriched zone containing internal oxides.

In this work, a two-step oxidation process is realized, combining a single-step oxidation of ultrafine-grained TiZrNbHfTa at 550 °C for 24 h in air with a vacuum heat treatment step at 1200 °C for 1 h, followed by water quenching, as shown in Fig. 1(a). According to the TiZrNbHfTa phase diagram in Fig. 1(b), 1200 °C is suitable for the formation of the single-phase bcc1 state. Both process steps are carried out in a laboratory furnace. For the vacuum heat treatment, specimens are encapsulated in an evacuated quartz glass tube (4×10^{3} Pa), as visible in Fig. 1(a). Figure 1(e) provides an overview micrograph of the resulting microstructure.

More detailed cross section images are investigated, obtained via backscattered electron imaging on a Zeiss 1540 ESB Cross Beam scanning electron microscope (SEM) equipped with a Thermo Noran System Six energy-dispersive X-ray spectroscopy (EDS) system. Figure 2(a) shows that the bulk microstructure after two-step oxidation is like that of coarse-grained single-phase bcc1 TiZrNbHFTa.[10,17] This does
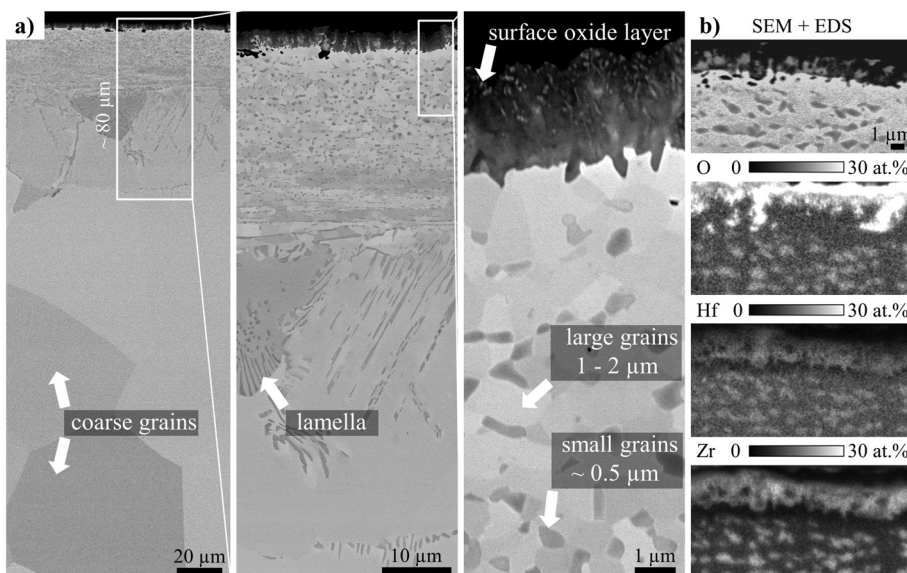

FIG. 2. (a) Detailed backscattered SEM images of TiZrNbHfTa after the two-step oxidation process with (b) corresponding EDS elemental mappings.
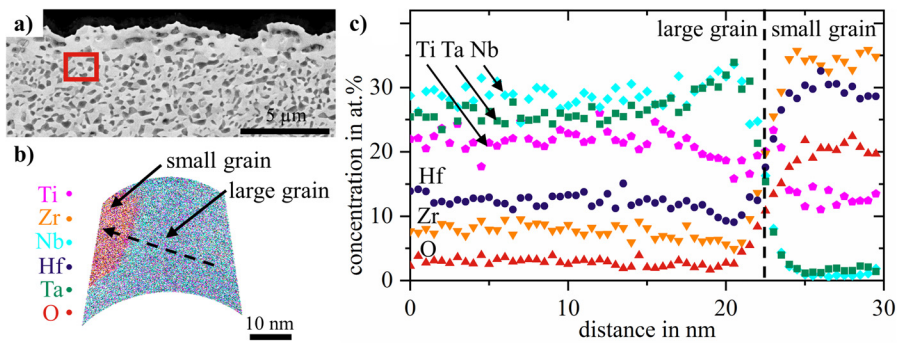
FIG. 3. (a) Visualization of the region from which APT needles are extracted, (b) cross section view of the analyzed region of interest covering an interface between a smaller and a larger grain, and (c) concentration profiles close to the interface as indicated by the dashed arrow in (b).

not apply to the microstructure in the upper $\sim 80\,\mu m$ close to the specimen surface. The backscattered SEM images reveal that a $2\,\mu m$ thick surface oxide layer is still present. Beneath, $1-2\,\mu m$ sized, larger grains with smaller, darker-appearing grains of $\sim 0.5\,\mu m$ size in between are apparent. After a depth of $\sim 25\,\mu m$ from the surface, the smaller, darker-appearing grains tend to occur in the form of lamella at the grain boundaries. According to the EDS mappings presented in Fig. 2(b), the smaller, darker-appearing grains are rich in Zr, Hf, and O. The high oxygen concentration above 30 at. % at the specimen surface indicates the presence of a surface oxide layer.

Closer composition analysis of the two-phase region is performed using a CAMECA LEAP 5000 XR atom probe tomography (APT) device. For this purpose, APT needles are prepared from the surface-near region, as indicated in Fig. 3(a). A concentration profile covering the interface between a smaller and a larger grain is extracted from the dataset, as shown in Fig. 3(b). Figure 3(c) shows the corresponding concentration profiles. Consistent with the EDS mappings, the $\sim 0.5\,\mu m$ sized, smaller grains are rich in Zr and Hf and contain a significant amount of ~ 20 at. % oxygen. Compared to the surrounding larger grains, they have less Ti, while they are completely depleted in

Nb and Ta. It is worth noting that also the Nb- and Ta-rich larger grains contain ~ 3 at. % of oxygen. The qualitative course of the respective concentration profiles at the interface is similar to those reported by Chen et al.[15] between a Nb- and Ta-rich bcc phase and a Hf- and Zr-rich hcp phase evolving due to a phase decomposition of single-phase TiZrNbHfTa at 700 °C. However, the relative elemental concentrations determined for the small and large grains in the subsurface region after two-step oxidation differ due to the additional presence of oxygen.

To investigate if the presence of oxygen is associated with the formation of internal oxides or if the oxygen is interstitially dissolved, X-ray photoelectron spectroscopy (XPS) is performed. For this purpose, the surface oxide layer is removed by grinding. This reveals the two-phase subsurface region, as shown in the SEM image in Fig. 4(a). After 200 min of sputtering with argon ions at 3 kV, the measurement is performed using a PHI 5000 VersaProbe III system. Figure 4(a) provides the XPS spectra according to which Ti, Nb, and Ta are present solely in the metallic state. Zr and Hf are also present dominantly in the metallic state, with minor amounts in the oxidized state. The formation of a native oxide layer on TiZrNbHfTa at ambient conditions,
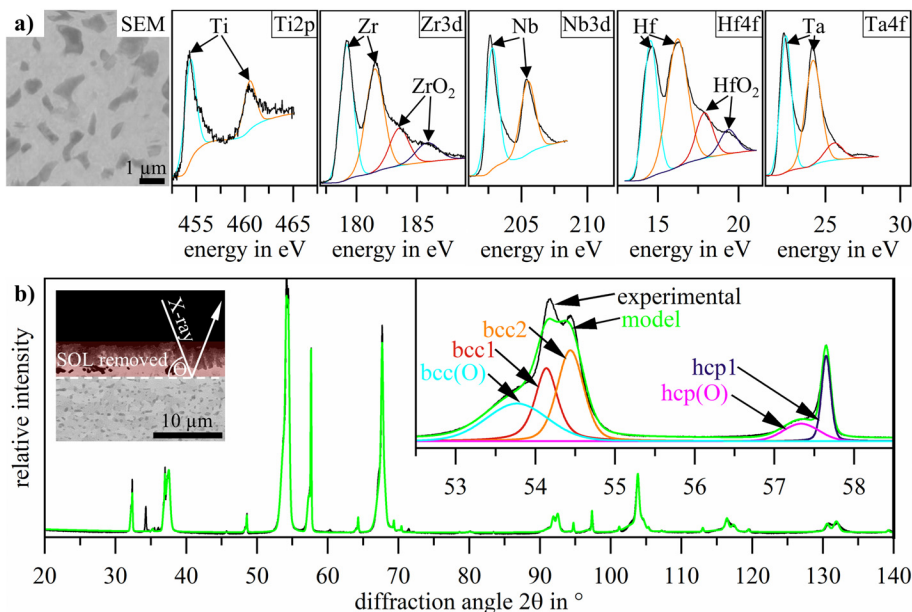

FIG. 4. (a) Surface XPS spectra of TiZrNbHfTa after two-step oxidation, mechanical removal of the surface oxide layer, and 200 min of sputtering with argon ions and (b) surface XRD diffractogram of TiZrNbHfTa after two-step oxidation and mechanical removal of the surface oxide layer (SOL), as schematically visualized, including a refinement model of the experimental data.
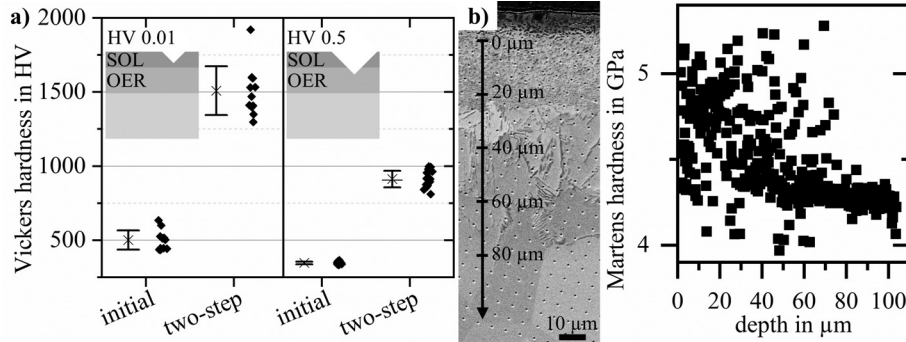
FIG. 5. (a) HV 0.01 and HV 0.5 Vickers surface hardness (mean, standard deviation, and data points) of TiZrNbHfTa in the initial state and after the two-step process and (b) Martens hardness-depth profile of the oxygen-enriched subsurface region determined on a specimen cross section, as indicated.

predominantly containing ZrO_2 and HfO_2,[19,20] underlines the high oxygen affinity of Zr and Hf. Such a high oxygen affinity can explain the occurrence of ZrO_2 and HfO_2 even after sputtering due to smallest quantities of oxygen remaining in the vacuum chamber during the XPS measurement. However, the dominance of peaks corresponding to the metallic state indicates that the oxygen is interstitially dissolved.

Interstitially dissolved oxygen in the subsurface region of TiZrNbHfTa after the two-step process is also suggested by an X-ray diffraction analysis (XRD) performed with a Bruker D8 discover using $CuK_{\alpha 1}$ monochromatic X-rays and a Bragg–Brentano setup. The measurement is done with a primary optics opening degree of 0.3° in the coupled theta/2theta mode covering the 2theta range 20°–140° at a step size of 0.01°. Figure 4(b) shows that besides reflections corresponding to the single-phase bcc1 bulk, the subsurface region is multiphase, containing an hcp1 and a bcc2 phase. Given the high oxygen solubility of hcp Ti,[21] Zr,[22,23] and Hf,[24,25] it is apparent that the oxygen-rich small grains have an hcp crystal structure, while the larger surrounding grains are bcc2. The magnified excerpt of the diffractogram in Fig. 4(b) reveals that the hcp and bcc reflections both exhibit pronounced asymmetric tails at the lower-angle side. These can be explained by a lattice distortion due to the interstitial oxygen. A shift of the positions of the reflections due to interstitial oxygen, associated with increased lattice constants, is confirmed for α-titanium alloys.[26,27] Also, for bcc TiZrNbHf, an increase in lattice constants due to oxygen dissolution has been reported.[28] Since the diffractogram convolutes information originating from different depths and the oxygen concentration decreases over depth, the observed asymmetric tails at the lower-angle side are plausible. To account for those in a Rietveld refinement model, an additional hcp(O) and bcc(O) phase is added.

Hardness measurements are performed to assess the effect of the two-step oxidation process on the surface hardness. Figure 5(a) depicts the results of HV 0.01 Vickers surface hardness measurements, performed using a Fischerscope HM 2000 microhardness tester, and of HV 0.5 measurements, performed using an Innovatest FALCON 500. In both cases, the surface oxide layer on top of an oxygen-enriched subsurface region significantly increases the hardness compared to the initial state. As schematically shown in Fig. 5(a), the indenter does not penetrate the surface oxide layer during HV 0.01 measurements, which is in contrast to the HV 0.5 measurements. This explains the higher surface hardness values obtained in the case of the HV 0.01 measurements, where only the oxides are measured that are typically harder than the metal they form from.[29,30] In addition to the Vickers surface hardness measurements, a series of depth-controlled ($0,2\,\mu m$) Martens

hardness measurements, also using a Fischerscope HM 2000, is realized on the cross section of a specimen after the two-step oxidation process. Figure 5(b) points out that the hardness decreases gradually over depth in the oxygen-enriched subsurface region, while the bulk hardness is constant. This is also observed for oxygen-enriched subsurface regions in, e.g., titanium alloys, where there is a correlation between oxygen concentration, also decreasing over depth, and hardness.[26,31] The large data scatter in the oxygen-enriched subsurface region is due to the presence of hcp1 and bcc2 grains, with the hcp grains having a higher hardness.

This work shows that the vacuum heat treatment during the two-step process can restore the single-phase bcc nature of the TiZrNbHfTa bulk material after single-step oxidation in air. The subsurface region, containing internal oxides after single-step oxidation, is altered to an hcp1/bcc2 two-phase region with interstitially dissolved oxygen. Known as an hcp phase stabilizing element in Ti, Zr, and Hf, oxygen in TiZrNbHfTa stabilizes the two-phase state compared to the single-phase bcc1 state. At the same time, the presence of a surface oxide layer is maintained. This surface oxide layer has a much higher hardness of 1509 ± 164 HV 0.01 (± standard deviation) compared to the untreated ultrafine-grained TiZrNbHfTa with a hardness of 501 ± 65 HV 0.01, which is beneficial for tribological applications.

AUTHOR DECLARATIONS
Conflict of Interest

The authors have no conflicts to disclose.

Author Contributions

Daniel Dickes: Conceptualization (equal); Data curation (lead); Investigation (equal); Methodology (lead); Project administration

10 February 2025 08:50:21

DATA AVAILABILITY

The data that support the findings of this study are available from the corresponding author upon reasonable request.

REFERENCES

[1]O. N. Senkov, J. M. Scott, S. V. Senkova, D. B. Miracle, and C. F. Woodward, "Microstructure and room temperature properties of a high-entropy TaNbHfZrTi alloy," J. Alloys Compd. **509**(20), 6043–6048 (2011).

[2]J. P. Couzinié, G. Dirras, L. Perrière, T. Chauveau, E. Leroy, Y. Champion, and I. Guillot, "Microstructure of a near-equimolar refractory high-entropy alloy," Mater. Lett. **126**, 285–287 (2014).

[3]G. Dirras, L. Lilensten, P. Djemia, M. Laurent-Brocq, D. Tingaud, J.-P. Couzinié, L. Perrière, T. Chauveau, and I. Guillot, "Elastic and plastic properties of as-cast equimolar TiHfZrTaNb high-entropy alloy," Mater. Sci. Eng., A **654**, 30–38 (2016).

[4]O. N. Senkov and S. L. Semiatin, "Microstructure and properties of a refractory high-entropy alloy after cold working," J. Alloys Compd. **649**, 1110–1123 (2015).

[5]G. Dirras, J. Gubicza, A. Heczel, L. Lilensten, J.-P. Couzinié, L. Perrière, I. Guillot, and A. Hocini, "Microstructural investigation of plastically deformed Ti$_{20}$Zr$_{20}$Hf$_{20}$Nb$_{20}$Ta$_{20}$ high entropy alloy by x-ray diffraction and transmission electron microscopy," Mater. Charact. **108**, 1–7 (2015).

[6]C.-C. Juan, K.-K. Tseng, W.-L. Hsu, M.-H. Tsai, C.-W. Tsai, C.-M. Lin, S.-K. Chen, S.-J. Lin, and J.-W. Yeh, "Solution strengthening of ductile refractory HfMo$_x$NbTaTiZr high-entropy alloys," Mater. Lett. **175**, 284–287 (2016).

[7]B. Guennec, V. Kentheswaran, L. Perrière, A. Ueno, I. Guillot, J.-P. Couzinié, and G. Dirras, "Four-point bending fatigue behavior of an equimolar BCC HfNbTaTiZr high-entropy alloy: Macroscopic and microscopic viewpoints," Materialia **4**, 348–360 (2018).

[8]M. Gueye, S. Ammar-Merah, S. Nowak, P. Decorse, A. Chevillot-Biraud, L. Perrière, J. P. Couzinie, I. Guillot, and G. Dirras, "Study of the stability under in vitro physiological conditions of surface silanized equimolar HfNbTaTiZr high-entropy alloy: A first step toward bio-implant applications," Surf. Coat. Technol. **385**, 125374 (2020).

[9]M. Geetha, A. K. Singh, R. Asokamani, and A. K. Gogia, "Ti based biomaterials, the ultimate choice for orthopaedic implants – A review," Prog. Mater. Sci. **54**(3), 397–425 (2009).

[10]D. Dickes, B. Öztürk, F. Baier, P. Berger, E. P. George, R. Völkl, M. C. Galetz, and U. Glatzel, "Surface hardening of TiZrNbHfTa high entropy alloy via oxidation," Corros. Sci. **217**, 111159 (2023).

[11]C.-H. Chang, M. S. Titus, and J.-W. Yeh, "Oxidation behavior between 700 and 1300 °C of refractory TiZrNbHfTa high-entropy alloys containing aluminum," Adv. Eng. Mater. **20**(6), 1700948 (2018).

[12]S. Sheikh, M. K. Bijaksana, A. Motallebzadeh, S. Shafeie, A. Lozinko, L. Gan, T.-K. Tsao, U. Klement, D. Canadinc, H. Murakami, and S. Guo, "Accelerated oxidation in ductile refractory high-entropy alloys," Intermetallics **97**, 58–66 (2018).

[13]B. Gorr, S. Schellert, F. Müller, H.-J. Christ, A. Kauffmann, and M. Heilmaier, "Current status of research on the oxidation behavior of refractory high entropy alloys," Adv. Eng. Mater. **23**, 2001047 (2021).

[14]B. Schuh, B. Völker, J. Todt, N. Schell, L. Perrière, J. Li, J. P. Couzinié, and A. Hohenwarter, "Thermodynamic instability of a nanocrystalline, single-phase TiZrNbHfTa alloy and its impact on the mechanical properties," Acta Mater. **142**, 201–212 (2018).

[15]S. Y. Chen, Y. Tong, K.-K. Tseng, J.-W. Yeh, J. D. Poplawsky, J. G. Wen, M. C. Gao, G. Kim, W. Chen, Y. Ren, R. Feng, W. D. Li, and P. K. Liaw, "Phase transformations of HfNbTaTiZr high-entropy alloy at intermediate temperatures," Scr. Mater. **158**, 50–56 (2019).

[16]S.-M. Chen, Z.-J. Ma, S. Qiu, L.-J. Zhang, S.-Z. Zhang, R. Yang, and Q.-M. Hu, "Phase decomposition and strengthening in HfNbTaTiZr high entropy alloy from first-principles calculations," Acta Mater. **225**, 117582 (2022).

[17]C. Gadelmeier, Y. Yang, U. Glatzel, and E. P. George, "Creep strength of refractory high-entropy alloy TiZrHfNbTa and comparison with Ni-base superalloy CMSX-4," Cell Rep. Phys. Sci. **3**, 100991 (2022).

[18]N. D. Stepanov, N. Yurchenko, S. V. Zherebtsov, M. A. Tikhonovsky, and G. A. Salishchev, "Aging behavior of the HfNbTaTiZr high entropy alloy," Mater. Lett. **211**, 87–90 (2018).

[19]J. Jayaraj, C. Thinaharan, S. Ningshen, C. Mallika, and U. K. Mudali, "Corrosion behavior and surface film characterization of TaNbHfZrTi high entropy alloy in aggressive nitric acid medium," Intermetallics **89**, 123–132 (2017).

[20]P. Hruška, F. Lukáč, S. Cichoň, M. Vondráček, J. Čížek, L. Fekete, J. Lančok, J. Veselý, P. Minárik, M. Cieslar, O. Melikhova, T. Kmječ, M. O. Liedke, M. Butterling, and A. Wagner, "Oxidation of amorphous HfNbTaTiZr high entropy alloy thin films prepared by DC magnetron sputtering," J. Alloys Compd. **869**, 157978 (2020).

[21]H. Okamoto, "O-Ti (Oxygen-Titanium)," J. Phase Equilib. Diffus. **32**(5), 473–474 (2011).

[22]C. Wang, M. Zinkevich, and F. Aldinger, "On the thermodynamic modeling of the Zr–O system," Calphad **28**(3), 281–292 (2004).

[23]J. P. Abriata, J. Garcés, and R. Versaci, "The O−Zr (Oxygen-Zirconium) system," Bull. Alloy Phase Diagrams **7**(2), 116–124 (1986).

[24]E. Rudy and P. Stecher, "Zum aufbau des systems hafnium-sauerstoff," J. Less Common Met. **5**(1), 78–89 (1963).

[25]H. Okamoto, "Hf-O (Hafnium-Oxygen)," in *Binary Alloy Phase Diagrams*, edited by T. B. Massalski, H. Okamoto, P. R. Subramanian, and L. Kacprzak (ASM International, Metals Park, Ohio, 1990).

[26]J. Baillieux, D. Poquillon, and B. Malard, "Observation using synchrotron x-ray diffraction of the crystallographic evolution of α-titanium after oxygen diffusion," Philos. Mag. Lett. **95**(5), 245–252 (2015).

[27]M. Berthaud, I. Popa, R. Chassagnon, O. Heintz, J. Lavková, and S. Chevalier, "Study of titanium alloy Ti6242S oxidation behaviour in air at 560 °C: Effect of oxygen dissolution on lattice parameters," Corros. Sci. **164**, 108049 (2020).

[28]Y. X. Ye, B. Ouyang, C. Z. Liu, G. J. Duscher, and T. G. Nieh, "Effect of interstitial oxygen and nitrogen on incipient plasticity of NbTiZrHf high-entropy alloys," Acta Mater. **199**, 413–424 (2020).

[29]J. F. Shackelford and W. Alexander, *CRC Materials Science and Engineering Handbook* (CRC Press, 2000).

[30]*Handbook of the Physicochemical Properties of the Elements*, edited by G. V. Samsonov (Springer International Publishing, Cham, 2012).

[31]D. Dickes, B. Öztürk, R. Völkl, M. C. Galetz, and U. Glatzel, "Improving the adhesion of a hard oxide layer on Ti6Al4V by a three-step thermal oxidation process," Adv. Eng. Mater. **24**, 2100864 (2021).

10 February 2025 08:50:21